Strong-Field Ionization of Helium

Qualifying Exam

Chuan Yu
201401656

Supervisor: Lars Bojer Madsen

November 2015

Department of Physics and Astronomy
Graduate School of Science and Technology
Aarhus University

Preface

This progress report contains some of the work done during part A of my Ph.D. studies at the Department of Physics and Astronomy, Aarhus University.

My project is about theoretical study of electron correlation in strong-field and attosecond physics. So far the work focuses on two-electron systems. This report displays numerical studies of strong-field ionization of a helium atom. The two-electron dynamics in the presence of intense laser pulses is studied by solving the time-dependent Schrödinger equation (TDSE) and extracting the ionization probability. All the computations are implemented in FORTRAN.

Notation

Atomic units $4\pi\epsilon_0 = \hbar = m_e = |e| = 1$ are used throughout this report unless stated otherwise.

Acknowledgements

I would like to thank my supervisor Lars Bojer Madsen for his excellent guidance: it is always beneficial to discuss with him. I would also like to thank all the group members for their kind help during my work.

Contents

Chapter 1

Introduction

The interaction of atomic and molecular systems with laser fields has been studied for several decades, both theoretically and experimentally. Such studies give knowledge about the structures and dynamics of the systems. With significant developments in laser technology during the past decades, new light sources with field strengths comparable to the Coulomb interaction in atoms and molecules are readily available. In such strong fields, the traditional perturbation theory breaks down, resulting in a number of new phenomena, such as above threshold ionization (ATI) [1], high harmonic generation (HHG) [2], ionization stabilization [3], etc. Studies on these strong-field phenomena also promote the development of the non-perturbative theoretical methods. On the other hand, laser pulses with durations in the femtosecond (fs) or even the attosecond (as) time regime, open up the possibility to observe and to control dynamics of atoms and molecules on their natural time scales, and give birth to entirely new research areas such as femtochemistry and attophysics [4].

In both theoretical formulation and numerical calculation, it is challenging to describe realistic multi-electron systems in strong-field physics. Due to the difficulty of completely describing multi-electron systems, the single-active electron (SAE) approximation [5] is often used in the strong-field regime. For example, a semi-classical three-step model can be used to qualitatively understand the HHG [2], i.e. the generation of high-energy photons with frequencies being a multiple of the laser frequency during the nonlinear interaction between laser and medium. In this model, first, a single electron is freed into the continuum via tunneling ionization; second, it is driven back and forth by the periodic laser field, accumulating energy from the field; third, at a later time it recombines with the parent ion with the excess energy emitted as a high energy photon. This model gives an explanation of the HHG cutoff, which is the binding energy plus the maximum kinetic energy obtained from the field.

However, it is increasingly realized that electron correlation can play an important role in strong-field and attosecond physics. To investigate the role of electron correlation in laser-induced dynamics, we have to go beyond the SAE approximation. The huge dimensionality and the large-amplitude electron motion in the strong-field regime make it difficult to numerically solve the time-dependent Schrödinger equation (TDSE). Several approaches have been developed for correlated many-electron systems, e.g., the time-dependent R-matrix (TD-RM) [6, 7, 8] approach, the multi-configurational time-dependent Hartree-Fock (MCTDHF) [9, 10] approach, the time-dependent restricted-active-space configuration-interaction (TD-RASCI) [11] approach, the time-dependent restricted-active-space self-consistent-field (TD-RASSCF) [12, 13] approach, etc. These methods are usually used to study processes in which only one electron is freed to the

continuum, since treatment of a double-continuum wavefunction is much more difficult.

Even for the simplest two-electron systems, such as He and H_2, the strong-field induced dynamics are not completely understood. At the current stage, my study is focused on the ionization of He in strong laser fields. It is possible to numerically solve the three-dimensional (3D) TDSE of He, with electron correlation fully included without any approximation. However, in the presence of intense laser fields, solving the 3D TDSE of He calls for a huge numerical grid with many discretization points, which is still a formidable task. To avoid the computational difficulty, we use a one-dimensional (1D) model for the interaction with linearly polarized laser, in which the two electrons are restricted to the direction of laser electric-field polarization. This 1D model is often used, since it can simplify the calculation and it keeps the essential physics.

For ionization, it is interesting to study the photoelectron spectra and the ionization probabilities. The time-dependent surface flux (t-SURFF) method was introduced to extract ionization spectra of one and two-electron atomic systems from numerical TDSE calculations, using a minimal simulation grid [14, 15]. Recently it was also extended to treat dissociation and dissociative ionization processes of H_2^+ [16]. In my work, the t-SURFF method is used to calculate the spectra of single ionization (in different channels) and double ionization, and then the corresponding probabilities.

This report centers around the strong-field ionization of helium. Chapter 2 introduces the numerical methods used in solving the TDSE, including the t-SURFF method for extracting the photoelectron spectra. In Chapter 3 we present and discuss some results for high frequency laser pulses, in which stabilization against ionization occurs. The high-frequency Floquet theory (HFFT) for stabilization is also outlined. Finally, Chapter 4 gives a summary of my work progress, and proposes an outlook and plans for the future.

Chapter 2

Numerical Methods

In this chapter we describe the numerical methods used in solving the TDSE, taking the 1D helium model as an example. Discretization of coordinate space, time propagation of wavefunction and calculation of spectra are discussed.

2.1 Discretization

With the coordinates of the two electrons of the 1D helium model denoted by x and y, we can express the time-independent field-free Hamiltonian as

$$\begin{aligned}\hat{H}_0 &= -\frac{1}{2}\frac{\partial^2}{\partial x^2} - \frac{1}{2}\frac{\partial^2}{\partial y^2} - \frac{2}{\sqrt{x^2+a_{en}}} - \frac{2}{\sqrt{y^2+a_{en}}} + \frac{1}{\sqrt{(x-y)^2+a_{ee}}} \\ &= \hat{T}_x + \hat{T}_y + V_x + V_y + V_{xy},\end{aligned} \tag{2.1}$$

where a_{en} and a_{ee} are softening parameters used to avoid the Coulomb singularity.

Within the dipole approximation, the time-dependent laser-interaction term in the length gauge (LG) and the velocity gauge (VG) is written as,

$$\hat{H}_1(t) = \hat{H}_x^L(t) + \hat{H}_y^L(t) = \begin{cases} F(t)\cdot(x+y) & \text{for the LG,} \\ A(t)\cdot(\hat{p}_x+\hat{p}_y) & \text{for the VG,} \end{cases} \tag{2.2}$$

where the electric field $F(t)$ and the vector potential $A(t)$ are related by $F(t) = -\partial_t A(t)$.

To solve the TDSE

$$i\partial_t\big|\Psi\big\rangle = \hat{H}\big|\Psi\big\rangle = (\hat{H}_0+\hat{H}_1)\big|\Psi\big\rangle, \tag{2.3}$$

the first step is discretization, i.e., setting up a basis set for the states.

Discrete Variable Representation

Instead of simply using discrete values of spatial coordinate variables, the discrete variable representation (DVR) [17] uses analytic basis functions localized about discrete values of the variables, which is an accurate and popular way to describe wavefunctions in numerical computations. Matrices of differential operators, e.g., the kinetic energy operator, are calculated analytically without having to resort to numerical approximation of derivatives, while matrices of coordinate operators, e.g., the potential energy operator, are diagonal and approximated by their values at the DVR points with Gaussian

quadrature accuracy. For a given number of points and weights, the Gaussian quadrature gives a good approximation to an integral. This contributes to the accuracy and efficiency of the DVR method.

For example, if we use N Gauss-Legendre quadrature points x_k and weights w_k, for integration on the interval $[a, b]$, we can construct a set of orthonormal basis functions from Lagrange interpolation polynomials

$$\chi_k(x) = \frac{1}{\sqrt{w_k}} \prod_{l \neq k} \frac{x - x_l}{x_k - x_l}. \tag{2.4}$$

Then the local potential energy matrix is diagonal in the DVR basis,

$$\begin{aligned} \big\langle \chi_k \big| V \big| \chi_l \big\rangle &= \int_a^b \chi_k(x) V(x) \chi_l(x) dx \approx \sum_{m=0}^{N-1} w_m \chi_k(x_m) V(x_m) \chi_l(x_m) \\ &= \sum_{m=0}^{N-1} w_m \frac{\delta_{mk}}{\sqrt{w_k}} V(x_m) \frac{\delta_{ml}}{\sqrt{w_l}} = \delta_{kl} V(x_k). \end{aligned} \tag{2.5}$$

The kinetic energy matrix is full, but its elements have analytic expressions.

Finite-Element Discrete Variable Representation

In our work, the finite-element discrete variable representation (FEDVR) basis is used, which is a more efficient basis set giving a kinetic energy matrix with a banded structure. Briefly speaking, the coordinate space is divided into a chosen number N_e of finite elements. In each element e, a grid of Gauss-Lobatto nodes x_k^e and integration weights w_k^e is set up, with the number of grid-points in element e denoted by n_e. Details of the grid setup can be found in Ref. [18].

Gauss-Lobatto nodes have the property that grid points are situated at the boundary of the finite element which accounts for the continuity of the wavefunction across two elements. The basis functions are constructed as Lagrange polynomials over the grid points in a chosen finite element,

$$\chi_k^e(x) = \frac{f_k^e(x)}{\sqrt{w_k^e}} \quad (k = 1, \ldots, n_e - 2), \tag{2.6}$$

where the Lobatto shape functions are defined by

$$f_k^e(x) = \prod_{l \neq k} \frac{x - x_l^e}{x_k^e - x_l^e}. \tag{2.7}$$

Further, at the boundary points of the finite element, i.e., at the grid-point $x_{n_e-1}^e = x_0^{e+1}$, we define a bridge function by

$$\chi_{n_e-1}^e(x) = \frac{f_{n_e-1}^e(x) + f_0^{e+1}(x)}{\sqrt{w_{n_e-1}^e + w_0^{e+1}}}, \tag{2.8}$$

which connects the finite elements e and $e + 1$.

The FEDVR then satisfies the usual property of DVR, i.e., a diagonal representation of local operators and a kinetic matrix having analytical expression [19],

$$V_{kl}^{ef} = \int \chi_k^e(x) V(x) \chi_l^f(x) dx \approx \delta_{ef}\delta_{kl} V(x_k^e), \tag{2.9}$$

$$T_{kl}^{ef} = \frac{\delta_{e,f} + \delta_{e,f\pm1}}{2} \int dx \frac{d}{dx}\chi_k^e(x) \frac{d}{dx}\chi_l^f(x). \tag{2.10}$$

Instead of using the element index e and the local DVR index k as in Eq. (2.6), we use a global index j for the FEDVR basis $\big|\chi_j\big\rangle$ in practice. Thus a 1D state is described as

$$\big|\psi\big\rangle = \sum_j \big|\chi_j\big\rangle\big\langle\chi_j\big|\psi\big\rangle \tag{2.11}$$

with

$$\sum_j \big|\chi_j\big\rangle\big\langle\chi_j\big| = 1. \tag{2.12}$$

Eq. (2.11) and Eq. (2.12) are exact for a complete basis set, which is not possible in practical computations, since we always use a limited number of basis functions in numerical calculations. With a basis set describing the wavefunction accurately, however, we may say that Eq. (2.11) and Eq. (2.12) are exact to the numerical accuracy.

So the n-th derivative of wavefunction can be easily evaluated by

$$\frac{d^n}{dx^n}\big\langle x\big|\psi\big\rangle = \sum_j \left(\frac{d^n}{dx^n}\big\langle x\big|\chi_j\big\rangle\right)\big\langle\chi_j\big|\psi\big\rangle. \tag{2.13}$$

Since the basis function $\chi_j(x) = \big\langle x\big|\chi_j\big\rangle$ is localized within only one (for an inner-element function like Eq. (2.6)) or two (for a bridge function like Eq. (2.8)) elements, evaluation of Eq. (2.13) at a point only calls for $\big\langle\chi_j\big|\psi\big\rangle$ corresponding to the one or two elements. Also the kinetic energy matrix evaluated via analytic differentiation of the basis functions shows an interesting sparse property.

As an example, we shows two connected finite elements [-2,0], [0,2] and seven FEDVR functions in Fig. 2.1. Then the corresponding kinetic energy matrix can be expressed in the following form,

$$\mathbf{T} = \begin{bmatrix} t_{11} & t_{12} & t_{13} & t_{14} & & & \\ t_{21} & t_{22} & t_{23} & t_{24} & & & \\ t_{31} & t_{32} & t_{33} & t_{34} & & & \\ t_{41} & t_{42} & t_{43} & t_{44} & t_{45} & t_{46} & t_{47} \\ & & & t_{54} & t_{55} & t_{56} & t_{57} \\ & & & t_{64} & t_{65} & t_{66} & t_{67} \\ & & & t_{74} & t_{75} & t_{76} & t_{77} \end{bmatrix}. \tag{2.14}$$

Sparse Matrix Manipulation

For a sparse matrix like Eq. (2.14), substantial memory requirement reductions can be realized by storing only the non-zero entries. Here we use two typical formats, the Compressed Sparse Row (CSR or CRS) and the Compressed Sparse Column (CSC or CCS) formats. Both these two formats are efficient for matrix-vector products, which are of fundamental importance in our calculations. Evaluation of any expectation value in quantum mechanics requires multiplication of the operator matrix on the state vector.

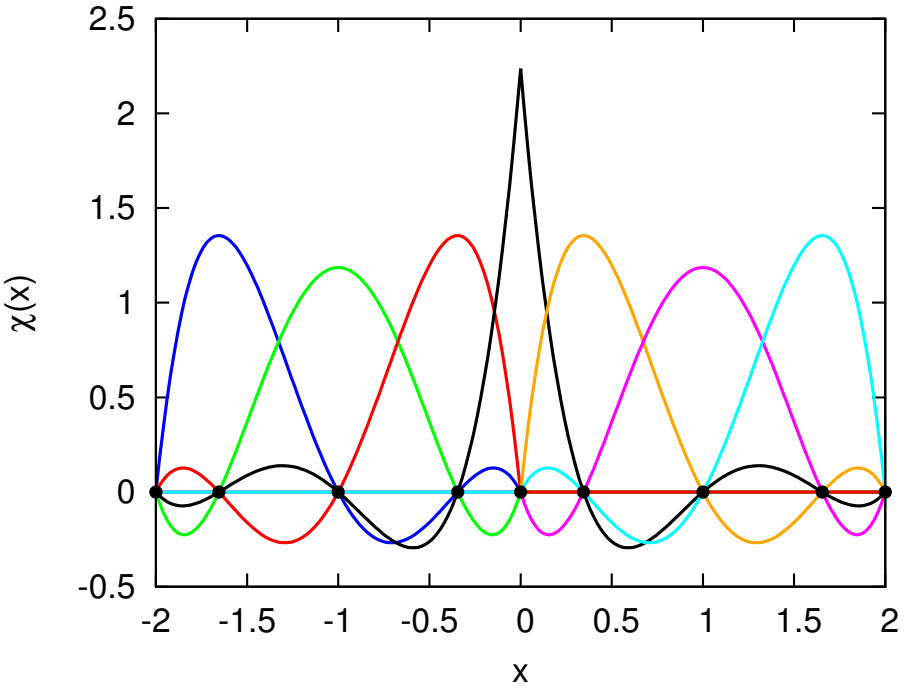

Figure 2.1: Two connected finite elements [-2,0], [0,2] and seven FEDVR functions. $\chi(x)$ stands for the FEDVR functions defined by Eq. (2.6) and Eq. (2.8).

As will be shown later, matrix-vector products also need to be computed in each time step when using the Arnoldi-Lanczos propagator.

The CRS format is (*val*, *col_ind*, *row_ptr*), where *val* is an array of the (left-to-right, then top-to-bottom) non-zero values of the matrix; *col_ind* records the column indexes corresponding to the values; and, *row_ptr* is the list of *val* indexes where each row starts.

The CSC format, similar to CSR, is (*val*, *row_ind*, *col_ptr*), where *val* is an array of the (top-to-bottom, then left-to-right) non-zero values of the matrix; *row_ind* records the row indexes corresponding to the values; and, *col_ptr* is the list of *val* indexes where each column starts.

Usually we have Hermitian or symmetric matrices, for which we only need to store half of the matrices in memory. In my implementation, the diagonal elements are stored as a vector, and the upper off-diagonal elements in the CSR format. Taking $\mathbf{T}$ in Eq. (2.14) for example, its upper off-diagonal sparse part is stored as

$$\begin{aligned} val &= [t_{12}, t_{13}, t_{14}, t_{23}, t_{24}, t_{34}, t_{45}, t_{46}, t_{47}, t_{56}, t_{57}, t_{67}], \\ col\_ind &= [2, 3, 4, 3, 4, 4, 5, 6, 7, 6, 7, 7], \\ row\_ptr &= [1, 4, 6, 7, 10, 12, 12]. \end{aligned}$$

The same *row_ptr* just indicates a row with all elements being zero, e.g., the *row_ptr* of the last row is the same as that of the last but one, due to the upper off-diagonal matrix.

We notice that this upper off-diagonal matrix has nice block structure, which is more convenient to manipulate. Considering matrix-vector multiplication, such a block (partitioned) matrix enables us to run the program in parallel easily.

If $\mathbf{T}$ is symmetric, the same storage can also be seen as the lower off-diagonal sparse part in the CSC format. With matrix-vector multiplication algorithms for the CSR and

CSC formats, the product of the matrix $\mathbf{T}$ and a vector $\mathbf{v}$ can be decomposed into three parts, $\mathbf{Tv} = \mathbf{T}^{diag}\mathbf{v} + \mathbf{T}^{upper}\mathbf{v} + \mathbf{T}^{lower}\mathbf{v}$.

Two-Electron Hamiltonian Matrices

For our two-electron problem, the same FEDVR functions are used for the two electrons x and y, with independent indexes ix and iy, i.e., $\chi_{ix}(x) = \langle x|\chi^x_{ix}\rangle$ and $\chi_{iy}(y) = \langle y|\chi^y_{iy}\rangle$, [1] so the basis set for the two-electron problem is labeled by two indexes ix and iy, $\chi_{ix}(x)\chi_{iy}(y)$.

Labeling the matrix elements by four indexes (ix, iy, jx, jy), we can calculate the matrices of all the operators in Eq. (2.1),

$$\langle\chi^x_{ix}|\langle\chi^y_{iy}|\hat{T}_x|\chi^x_{jx}\rangle|\chi^y_{jy}\rangle = \langle\chi^x_{ix}|\hat{T}_x|\chi^x_{jx}\rangle\langle\chi^y_{iy}|\chi^y_{jy}\rangle = (\mathbf{T}_x)_{ix,jx}\delta_{iy,jy}, \tag{2.15}$$

$$\langle\chi^x_{ix}|\langle\chi^y_{iy}|\hat{T}_y|\chi^x_{jx}\rangle|\chi^y_{jy}\rangle = \langle\chi^y_{iy}|\hat{T}_y|\chi^y_{jy}\rangle\langle\chi^x_{ix}|\chi^x_{jx}\rangle = (\mathbf{T}_y)_{iy,jy}\delta_{ix,jx}, \tag{2.16}$$

$$\langle\chi^x_{ix}|\langle\chi^y_{iy}|V_x|\chi^x_{jx}\rangle|\chi^y_{jy}\rangle = \langle\chi^x_{ix}|V_x|\chi^x_{jx}\rangle\langle\chi^y_{iy}|\chi^y_{jy}\rangle = V_x(x_{ix})\delta_{ix,jx}\delta_{iy,jy}, \tag{2.17}$$

$$\langle\chi^x_{ix}|\langle\chi^y_{iy}|V_y|\chi^x_{jx}\rangle|\chi^y_{jy}\rangle = \langle\chi^y_{iy}|V_y|\chi^y_{jy}\rangle\langle\chi^x_{ix}|\chi^x_{jx}\rangle = V_y(y_{iy})\delta_{iy,jy}\delta_{ix,jx}, \tag{2.18}$$

$$\langle\chi^x_{ix}|\langle\chi^y_{iy}|V_{xy}|\chi^x_{jx}\rangle|\chi^y_{jy}\rangle = V_{xy}(x_{ix}, y_{iy})\delta_{ix,jx}\delta_{iy,jy}. \tag{2.19}$$

It shows that the matrix of kinetic energy operator is easy to manipulate, with only one sparse matrix stored in memory, while all the potential energy matrices are approximated by their values in the FEDVR.

2.2 Time Propagation

Time-Evolution Operator

Quantum-mechanical time-propagation evolves a given wavefunction at time t_0 to a new one at time t with preservation of the norm. Its action is thus expressed by a unitary time-evolution operator $U(t, t_0)$ defined by the relation

$$|\Psi(t)\rangle = \hat{U}(t, t_0)|\Psi(t_0)\rangle. \tag{2.20}$$

The equation of motion and the initial condition follow directly from the TDSE,

$$i\partial_t\hat{U}(t, t_0) = \hat{H}(t)\hat{U}(t, t_0), \tag{2.21}$$

$$\hat{U}(t_0, t_0) = 1. \tag{2.22}$$

And its solution can be written as,

$$\hat{U}(t, t_0) = \mathcal{T}\exp\left[-i\int_{t_0}^{t}\hat{H}(t')dt'\right] \approx \exp\left[-i\hat{H}(t_{M-1})\Delta t\right]\ldots\exp\left[-i\hat{H}(t_0)\Delta t\right], \tag{2.23}$$

where $\mathcal{T}$ is time-ordering operator.

For a short time step Δt, we can approximate the action of the time-evolution operator on the state with an exponential-type propagator,

$$|\Psi(t + \Delta t)\rangle = \exp\left[-i\hat{H}(t)\Delta t\right]|\Psi(t)\rangle, \tag{2.24}$$

With the dimension of wavefunction, i.e., the total number of the basis functions denoted by N, the matrix of $\hat{H}$ is $\mathbf{H}_{N\times N}$. Exact calculation of matrix exponential scales cubically with dimension, feasible only for small systems.

[1] In this chapter, we use the superscript x or y for a one-electron state, and the subscript x or y for a one-electron operator.

Arnoldi-Lanczos Scheme

Instead of evaluating the huge matrix exponential, the fundamental idea of Arnoldi-Lanczos method is to make use of the Krylov subspace, spanned by a small set of vectors $\hat{H}^k\big|\Psi\big\rangle, (k = 0, \ldots, L)$.

To begin with, we can expand Eq. (2.24) as

$$\big|\Psi(t + \Delta t)\big\rangle = \sum_{n=0}^{\infty}(n!)^{-1}\left[-i\hat{H}(t)\Delta t\right]^n\big|\Psi(t)\big\rangle, \tag{2.25}$$

For a short time step Δt that ensures the convergence of the series, we can truncate the expansion to some order,

$$\big|\Psi(t + \Delta t)\big\rangle \approx \sum_{n=0}^{L}(n!)^{-1}\left[-i\hat{H}(t)\Delta t\right]^n\big|\Psi(t)\big\rangle, \tag{2.26}$$

which means that we express the $\big|\Psi(t + \Delta t)\big\rangle$ by using $\hat{H}^k\big|\Psi\big\rangle, (k = 0, \ldots, L)$.

To illustrate the Krylov subspace method, we first use a general basis set $\big\{\big|\chi_j\big\rangle\big\}$ for the system and express the Hamiltonian as,

$$\hat{H} = \sum_j\sum_k\big|\chi_j\big\rangle\big\langle\chi_j\big|\hat{H}\big|\chi_k\big\rangle\big\langle\chi_k\big|, \tag{2.27}$$

where $\big\langle\chi_j\big|\hat{H}\big|\chi_k\big\rangle$ is the matrix element of the Hamiltonian $\mathbf{H}$. Similar to Eq. (2.12), Eq. (2.27) is understood to be exact to the numerical accuracy, as long as the state can be well described by the basis set.

Similarly, in the Krylov subspace spanned by $\hat{H}^k\big|\Psi\big\rangle, (k = 0, \ldots, L)$, we can find an orthonormal set of vectors $\big|Q_k\big\rangle, (k = 0, \ldots, L)$, and approximate the Hamiltonian as

$$\hat{H} \approx \sum_{j=0}^{L}\sum_{k=0}^{L}\big|Q_j\big\rangle\big\langle Q_j\big|\hat{H}\big|Q_k\big\rangle\big\langle Q_k\big|, \tag{2.28}$$

where $\big\langle Q_j\big|\hat{H}\big|Q_k\big\rangle$ is the matrix element of the reduced Hamiltonian $\mathbf{H_L}$.

Since Eq. (2.26) indicates that we express the $\big|\Psi(t + \Delta t)\big\rangle$ in the Krylov subspace,

$$\big|\Psi(t + \Delta t)\big\rangle \approx \sum_{j=0}^{L}\big|Q_j\big\rangle\big\langle Q_j\big|\Psi(t + \Delta t)\big\rangle, \tag{2.29}$$

Eq. (2.28) can be used as a substitute of Eq. (2.27) in short-time propagation. Thus the exponential-type propagator in Eq. (2.24) is approximated as

$$\begin{aligned}
\exp\left[-i\hat{H}\Delta t\right] &\approx \sum_{n=0}^{\infty}(n!)^{-1}\left[-i\Delta t\sum_{j=0}^{L}\sum_{k=0}^{L}\big|Q_j\big\rangle\big\langle Q_j\big|\hat{H}\big|Q_k\big\rangle\big\langle Q_k\big|\right]^n \\
&= \sum_{j=0}^{L}\sum_{k=0}^{L}\big|Q_j\big\rangle\left[\sum_{n=0}^{\infty}(n!)^{-1}(-i\Delta t\mathbf{H_L})^n\right]_{jk}\big\langle Q_k\big| \\
&= \sum_{j=0}^{L}\sum_{k=0}^{L}\big|Q_j\big\rangle\left[\exp\left(-i\Delta t\mathbf{H_L}\right)\right]_{jk}\big\langle Q_k\big|.
\end{aligned} \tag{2.30}$$

The orthonormal set $\{|Q_0\rangle, \ldots, |Q_L\rangle\}$ and the matrix $\mathbf{H_L}$ can be obtained with a modified Gram-Schmidt orthogonalization, i.e., the Arnoldi-Lanczos recursion. Starting from a normalized state $|Q_0\rangle = |\Psi(t)\rangle/\|\Psi(t)\| = |\Psi(t)\rangle/\sqrt{\langle\Psi(t)|\Psi(t)\rangle}$, it constructs an orthonormal basis $\{|Q_0\rangle, \ldots, |Q_L\rangle\}$ by a two-fold loop,

for $k = 0, \ldots, L$ **do**
  $|\Phi_{k+1}^{(0)}\rangle = \hat{H}|Q_k\rangle$
  for $j = 0, \ldots, k$ **do**
    $\beta_{jk} = \langle Q_j|\Phi_{k+1}^{(j)}\rangle$
    $|\Phi_{k+1}^{(j+1)}\rangle = |\Phi_{k+1}^{(j)}\rangle - |Q_j\rangle\beta_{jk}$
  end for
  $\beta_{k+1,k} = \|\Phi_{k+1}^{(k+1)}\| = \sqrt{\langle\Phi_{k+1}^{(k+1)}|\Phi_{k+1}^{(k+1)}\rangle}$
  $|Q_{k+1}\rangle = |\Phi_{k+1}^{(k+1)}\rangle/\beta_{k+1,k}$
end for

Then the reduced Hamiltonian $\mathbf{H_L}$ is a complex upper Hessenberg matrix of dimension $(L+1)\times(L+1)$, with its matrix elements given by

$$(\mathbf{H_L})_{jk} = \langle Q_j|\hat{H}|Q_k\rangle = \begin{cases} \beta_{jk} & \text{for} \quad j \le k+1, \\ 0 & \text{else.} \end{cases} \tag{2.31}$$

The small matrix of the reduced Hamiltonian $\mathbf{H_L}$ can be easily diagonalized with a similarity transformation,

$$\mathbf{S}^{-1}\mathbf{H_L}\mathbf{S} = \boldsymbol{\lambda} \tag{2.32}$$

where $\boldsymbol{\lambda} = diag(\lambda_0, \ldots, \lambda_L)$ is diagonal matrix of eigenvalues of $\mathbf{H}_L$ and $\mathbf{S}$ the corresponding eigenvector matrix of $\mathbf{H}_L$. Then the exponential of $\mathbf{H_L}$ is calculated by

$$\exp\left[-i\mathbf{H}_L\Delta t\right] = \mathbf{S}\exp[-i\boldsymbol{\lambda}\Delta t]\mathbf{S}^{-1} = \mathbf{S}diag(\exp[-i\lambda_0\Delta t], \ldots, \exp[-i\lambda_L\Delta t])\mathbf{S}^{-1}. \tag{2.33}$$

Finally we find the coefficents $c_j = \langle Q_j|\Psi(t+\Delta t)\rangle$ in Eq. (2.29)

$$\begin{aligned} c_j &= \langle Q_j|\exp\left(-i\hat{H}\Delta t\right)|\Psi(t)\rangle \\ &= \langle Q_j|\sum_{k=0}^{L}\sum_{l=0}^{L}|Q_k\rangle\left[\exp\left(-i\mathbf{H_L}\Delta t\right)\right]_{kl}\langle Q_l|Q_0\rangle\|\Psi(t)\| \\ &= \sum_{k=0}^{L}\left[\mathbf{S}\right]_{jk}\exp\left[-i\lambda_k\Delta t\right]\left[\mathbf{S}^{-1}\right]_{k0}\|\Psi(t)\|. \end{aligned} \tag{2.34}$$

We note that the Arnoldi-Lanczos algorithm requires $L+1$ evaluations of matrix-vector products in each time step. Combined with the FEDVR basis set, the sparse matrix of $\hat{H}$ leads to high efficiency. The derivations above consider a general state $|\Psi(t)\rangle$, which is not restricted to our 1D helium model. So the Arnoldi-Lanczos scheme can be generally applied to any multi-electron system.

Imaginary Time Propagation

The ground state, i.e., the state with the lowest energy, is obtained by performing the imaginary time propagation (ITP): one can start from a guessed wavefunction and

propagate it in this way,

$$\big|\Psi(\tau+\Delta\tau)\big\rangle = \exp\Big[-\hat{H}(\tau)\Delta\tau\Big]\,\big|\Psi(\tau)\big\rangle, \tag{2.35}$$

where normalization of $\big|\Psi(\tau)\big\rangle$ is needed in each time step.

After obtaining the ground state $\big|\Psi_0\big\rangle$ with high accuracy, we can redo the ITP and project out the ground state contribution from the wavefunction in each time step,

$$\big|\Psi(\tau+\Delta\tau)\big\rangle = \exp[-\hat{H}(\tau)\Delta\tau]\,\big[1-\big|\Psi_0\big\rangle\big\langle\Psi_0\big|\big]\,\big|\Psi(\tau)\big\rangle, \tag{2.36}$$

thus a state with the second-lowest energy will be obtained.

This procedure can be repeated to prepare a small number of bound states, which can be chosen as the initial condition for the real time propagation (RTP). However, the numerical error will be accumulated on each energy level. So we only use the ITP method for the ground state and the first excited spin-singlet (spatially-symmetric) state.

For our 1D helium model, with softening parameters $a_{en} = 0.5$ and $a_{ee} = 0.325$, the ground state energy is -2.90 a.u., which is a good approximation to that of a real helium atom.

Complex Absorbing Potentials

When interacting with a strong laser pulse, electrons can be liberated and travel large distances during and after the pulse. If electron wavepackets reach the grid boundaries in numerical calculations, unphysical reflections can occur, distorting the true physics.

To extract correct observables it is therefore crucial to make sure that the wave packets do not reach the boundary of the simulation volume. One method is the usage of complex absorbing potentials (CAPs) [20] near the box boundaries that can absorb the outgoing wavepackets without modifying the wavefunction in the inner part of the grid.

In our work, $V_{CAP}(x,y) = -iW_x - iW_y$ is added to the Hamiltonian in real time propagation, where W_x (or W_y) is a function of this form,

$$W_x = \begin{cases} 1-\cos\left[\frac{\pi(|x|-r_c)}{2(r_{max}-r_c)}\right] & \text{for} \quad r_c < |x| < r_{max} \\ 0 & \text{for} \quad |x| \le r_c \end{cases}. \tag{2.37}$$

2.3 Calculation of Ionization Spectra

To extract photoelectron spectra, the most straightforward approach is to project the final state onto the exact scattering states after the laser pulse. Instead of solving for the exact scattering states, we can approximate them by Volkov states in the asymptotic free zone where the Coulomb interactions can be neglected, and perform the projection only in the asymptotic region after long time propagation [21]. In the limit of infinitely long time and infinitely large grid, such a projection can give accurate results, since the freed electron is completely in the asymptotic region far from the core. The time-dependent surface flux (t-SURFF) method [14, 15] shows that such a projection can be related to the flux passing through some surfaces, which are the boundaries of the asymptotic region. By using the t-SURFF method, we can still extract photoelectron spectra with the wavefunction absorbed beyond the surfaces. Combined with efficient CAPs, it requires a small simulation box to analyze the momentum distribution of photoelectron.

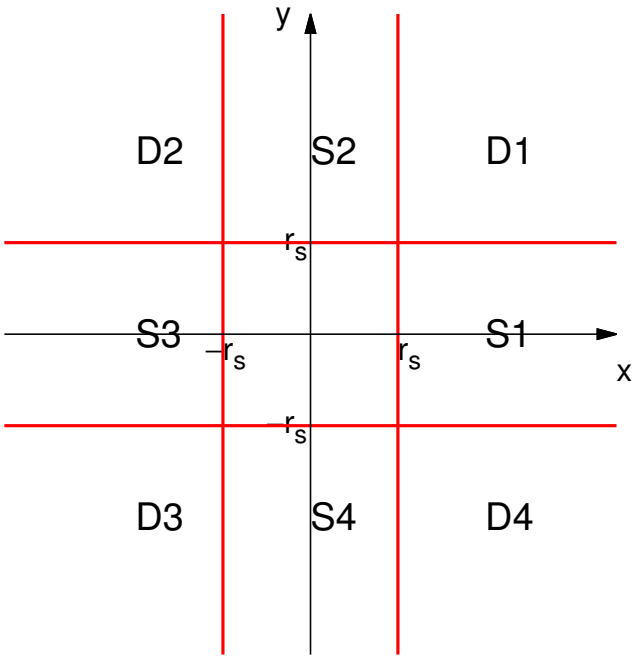

Figure 2.2: Partition of the coordinate space into bound and asymptotic regions

Partition of Coordinate Space

For 1D helium considered here, we can decompose the coordinate space into bound and asymptotic regions, as Fig. 2.2 shows. We consider single ionization into ionic channels and double ionization. In Fig. 2.2, the regions S1, S2, S3, S4 correspond to single ionization while the regions D1, D2, D3, D4 correspond to double ionization.

We assume that the electron-core interaction V_x (or V_y) can be neglected for $|x| > r_s$ (or $|y| > r_s$), and that the electron-electron interaction V_{xy} can be neglected for either $|x| > r_s$ or $|y| > r_s$.

For convenience, we define the following operators with Heaviside step functions $\theta(x)$ and $\theta(y)$,

$$\hat{\theta}_{+x} = \int dx|x\rangle\theta(+x - r_s)\langle x|, \qquad \hat{\theta}_{-x} = \int dx|x\rangle\theta(-x - r_s)\langle x|, \tag{2.38}$$

$$\hat{\theta}_{+y} = \int dy|y\rangle\theta(+y - r_s)\langle y|, \qquad \hat{\theta}_{-y} = \int dy|y\rangle\theta(-y - r_s)\langle y|, \tag{2.39}$$

which are used to describe projections in different regions.

Here we exemplify the t-SURFF method for single and double ionization in regions S1 and D1, corresponding to $\hat{\theta}_{+x}(1 - \hat{\theta}_{+y} - \hat{\theta}_{-y})$ and $\hat{\theta}_{+x}\hat{\theta}_{+y}$.

t-SURFF for Single Ionization

The Hamiltonian in the region S1 $\{x > r_s, |y| < r_s\}$ is approximated by

$$\hat{H}_{S1} = \hat{T}_x + \hat{H}_x^L + \hat{T}_y + \hat{V}_y + \hat{H}_y^L = \hat{H}_x^V + \hat{H}_y^I, \tag{2.40}$$

where $\hat{H}^V = \hat{T}_x + \hat{H}_x^L$ and $\hat{H}^I = \hat{T}_y + \hat{V}_y + \hat{H}_y^L$ stand for Volkov and ionic Hamiltonian, respectively.

Denoting the Volkov state of momentum k by $\big|\phi_k^x(t)\big\rangle$ and the ionic channel state c by $\big|\phi_c^y(t)\big\rangle$, we can write their corresponding TDSEs as

$$i\partial_t\big|\phi_k^x\big\rangle = \hat{H}_x^V\big|\phi_k^x\big\rangle, \tag{2.41}$$

$$i\partial_t\big|\phi_c^y\big\rangle = \hat{H}_y^I\big|\phi_c^y\big\rangle. \tag{2.42}$$

In Eq. (2.41), the Volkov wavefunction describing the motion of free electrons in the laser field is given by

$$\begin{aligned}&\big\langle x\big|\phi_k^x\big\rangle\\ &=\begin{cases}(2\pi)^{-1/2}\exp\{i[k+A(t)]x\}\exp\left\{-\int_\infty^t dt'[k^2/2+A(t')k+A(t')^2/2]\right\} & \text{for the LG,}\\ (2\pi)^{-1/2}\exp\{ikx\}\exp\left\{-\int_\infty^t dt'[k^2/2+A(t')k]\right\} & \text{for the VG.}\end{cases}\end{aligned} \tag{2.43}$$

In Eq. (2.42) $\big|\phi_c^y\big\rangle$ becomes a field-free ionic state when $t\to\infty$, so it can be solved by performing backward time propagation.

At a large time T, we can perform the projection in the region S1 $\{x>r_s,|y|<r_s\}$ to calculate the transition amplitude $a_{SI}(k,c,T)$,

$$a_{SI}(k,c,T) = \big\langle\phi_k^x(T)\big|\big\langle\phi_c^y(T)\big|\hat{\theta}_{+x}(1-\hat{\theta}_{+y}-\hat{\theta}_{-y})\big|\Psi(T)\big\rangle, \tag{2.44}$$

which means that one electron is freed with asymptotic momentum $k>0$ with the helium ion being in a bound state c. And the corresponding spectral intensity is defined by the probability $P_{SI}(k,c)=|a_{SI}(k,c,T)|^2$.

$a_{SI}(k,c,T)$ can also be expressed as,

$$\begin{aligned}a_{SI}(k,c,T) =& \int_{-\infty}^{T} dt\left\{\partial_t\big\langle\phi_k^x(t)\big|\big\langle\phi_c^y(t)\big|\hat{\theta}_{+x}(1-\hat{\theta}_{+y}-\hat{\theta}_{-y})\big|\Psi(t)\big\rangle\right\}\\ =& i\int_{-\infty}^{T} dt\left\{\big\langle\phi_k^x(t)\big|\big\langle\phi_c^y(t)\big|(\hat{H}_x^V+\hat{H}_y^I)\hat{\theta}_{+x}(1-\hat{\theta}_{+y}-\hat{\theta}_{-y})\big|\Psi(t)\big\rangle\right.\\ &\left.-\big\langle\phi_k^x(t)\big|\big\langle\phi_c^y(t)\big|\hat{\theta}_{+x}(1-\hat{\theta}_{+y}-\hat{\theta}_{-y})(\hat{H}_x^V+\hat{H}_y^I)\big|\Psi(t)\big\rangle\right\}.\end{aligned} \tag{2.45}$$

where we use the fact

$$\hat{\theta}_{+x}(1-\hat{\theta}_{+y}-\hat{\theta}_{-y})\hat{H}\big|\Psi(t)\big\rangle = \hat{\theta}_{+x}(1-\hat{\theta}_{+y}-\hat{\theta}_{-y})\hat{H}_{S1}\big|\Psi(t)\big\rangle, \tag{2.46}$$

since $\hat{H}_{S1}$ only neglects some potentials from the total Hamiltonian $\hat{H}$.

By assuming that $\big\langle y\big|\phi_c^y\big\rangle\approx 0$ for $|y|>r_s$, we may rewrite

$$\begin{aligned}a_{SI}(k,c,T) &= i\int_{-\infty}^{T} dt\big\langle\phi_k^x(t)\big|[\hat{H}_x^V,\hat{\theta}_{+x}]\big\langle\phi_c^y(t)\big|\Psi(t)\big\rangle\\ &= i\int_{-\infty}^{T} dt\sum_n\big\langle\phi_k^x(t)\big|[\hat{H}_x^V,\hat{\theta}_{+x}]\big|\chi_n^x\big\rangle\big\langle\chi_n^x\big|\big\langle\phi_c^y(t)\big|\Psi(t)\big\rangle\end{aligned} \tag{2.47}$$

where Eq. (2.12) is used for the electron labeled by x.

t-SURFF for Double Ionization

Similarly, we can perform the projection in the region D1 $\{x > r_s, y > r_s\}$ at a large time T to calculate the transition amplitude $a_{DI}(k_1, k_2, T)$,

$$\begin{aligned} a_{DI}(k_1,k_2,T) =& i\int_{-\infty}^{T} dt \left\{ \partial_t \langle \phi^x_{k_1}(t) | \langle \phi^y_{k_2}(t) | \hat{\theta}_{+x}\hat{\theta}_{+y} | \Psi(t)\rangle \right\} \\ =& i\int_{-\infty}^{T} dt \Big\{ \langle \phi^x_{k_1}(t) | \langle \phi^y_{k_2}(t) | (\hat{H}^V_x + \hat{H}^V_y)\hat{\theta}_{+x}\hat{\theta}_{+y} | \Psi(t)\rangle \\ & - \langle \phi^x_{k_1}(t) | \langle \phi^y_{k_2}(t) | \hat{\theta}_{+x}\hat{\theta}_{+y}(\hat{H}^V_x + \hat{H}^V_y) | \Psi(t)\rangle \Big\} \\ =& i\int_{-\infty}^{T} dt \Big\{ \langle \phi^x_{k_1}(t) | \langle \phi^y_{k_2}(t) | [\hat{H}^V_y, \hat{\theta}_{+y}]\hat{\theta}_{+x} | \Psi(t)\rangle \\ & + \langle \phi^x_{k_1}(t) | \langle \phi^y_{k_2}(t) | [\hat{H}^V_x, \hat{\theta}_{+x}]\hat{\theta}_{+y} | \Psi(t)\rangle \Big\}, \end{aligned} \tag{2.48}$$

which means that both electrons are freed with asymptotic momentum $k_1 > 0$ and $k_2 > 0$. And the corresponding probability is $P_{DI}(k_1, k_2) = |a_{DI}(k_1, k_2, T)|^2$.

We denote the integrand in Eq. (2.48) by $b(k_1, k_2, t) + \bar{b}(k_1, k_2, t)$. The two terms are related by exchange symmetry $b(k_1, k_2, t) = \bar{b}(k_2, k_1, t)$.

To evaluate

$$\begin{aligned} b(k_1,k_2,t) &= \langle \phi^x_{k_1}(t) | \langle \phi^y_{k_2}(t) | [\hat{H}^V_y, \hat{\theta}_{+y}]\hat{\theta}_{+x} | \Psi(t)\rangle \\ &= \sum_n \langle \phi^y_{k_2}(t) | [\hat{H}^V_y, \hat{\theta}_{+y}] | \chi^y_n\rangle \langle \chi^y_n | \langle \phi^x_{k_1}(t) | \hat{\theta}_{+x} | \Psi(t)\rangle, \end{aligned} \tag{2.49}$$

we define

$$b_1(k_1, n, t) = \langle \chi^y_n | \langle \phi^x_{k_1}(t) | \hat{\theta}_{+x} | \Psi(t)\rangle \tag{2.50}$$

and calculate it by solving the corresponding time-dependent equation,

$$\begin{aligned} i\partial_t b_1(k_1,n,t) =& \langle \chi^y_n | \langle \phi^x_{k_1}(t) | \hat{\theta}_{+x}(\hat{H}^V_x + \hat{H}^I_y) | \Psi(t)\rangle - \langle \chi^y_n | \langle \phi^x_{k_1}(t) | \hat{H}^V_x\hat{\theta}_{+x} | \Psi(t)\rangle \\ =& \langle \phi^x_{k_1}(t) | \hat{\theta}_{+x} \langle \chi^y_n | \hat{H}^I_y | \Psi(t)\rangle - \langle \phi^x_{k_1}(t) | [\hat{H}^V_x, \hat{\theta}_{+x}] \langle \chi^y_n | \Psi(t)\rangle \\ =& \sum_m \langle \chi^y_n | \hat{H}^I_y | \chi^y_m\rangle b_1(k_1, m, t) - \sum_m \langle \phi^x_{k_1}(t) | [\hat{H}^V_x, \hat{\theta}_{+x}] | \chi^x_m\rangle \langle \chi^x_m | \langle \chi^y_n | \Psi(t)\rangle. \end{aligned} \tag{2.51}$$

where Eq. (2.12) is used for the two electrons labeled by x and y.

t-SURFF with CAPs

The derivations above show that the t-SURFF method is equivalent to projecting the final wavefunction onto approximated scattering states in the asymptotic region after long-time propagation.

When implementing the t-SURFF method in numerical calculations, we assume that an ideal CAP of in x (or y) direction does not modify the wavefunction in the inner region of the grid $|x| < r_c$ (or $|y| < r_c$), and choose $r_c > r_s$.

Evaluation of the commutator

$$\begin{aligned}
&\big\langle f\big|[\hat{H}_x^V,\hat{\theta}_{+x}]\big|g\big\rangle \\
&=\begin{cases}
\frac{1}{2}\left[\frac{d\big\langle f\big|x\big\rangle}{dx}\big\langle x\big|g\big\rangle-\big\langle f\big|x\big\rangle\frac{d\big\langle x\big|g\big\rangle}{dx}\right]_{x=r_s} & \text{for the LG,}\\
\frac{1}{2}\left[\frac{d\big\langle f\big|x\big\rangle}{dx}\big\langle x\big|g\big\rangle-\big\langle f\big|x\big\rangle\frac{d\big\langle x\big|g\big\rangle}{dx}\right]_{x=r_s}-iA(t)\left[\big\langle f\big|x\big\rangle\big\langle x\big|g\big\rangle\right]_{x=r_s} & \text{for the VG,}
\end{cases}
\end{aligned} \tag{2.52}$$

only calls for the values and first derivatives of f and g at the point r_s. Therefore Eq. (2.47) for the single ionization is still valid with the CAPs included.

The formula for double ionization should be altered to include the CAPs in practical computation. To illustrate this, we consider the following equations,

$$i\partial_t\big|\tilde{\Psi}\big\rangle=[\hat{H}-iW_x-iW_y]\big|\tilde{\Psi}\big\rangle, \tag{2.53}$$

$$i\partial_t\big|\tilde{\Psi}_1\big\rangle=[\hat{H}-iW_y]\big|\tilde{\Psi}_1\big\rangle. \tag{2.54}$$

In Eq. (2.49), the existence of the commutator $[\hat{H}_y^V,\hat{\theta}_{+y}]$ allows us to replace $\big|\Psi\big\rangle$ by $\big|\tilde{\Psi}_1\big\rangle$.

Similar to Eq. (2.50), we define

$$\tilde{b}_1(k_1,n,t)=\big\langle\chi_n^y\big|\big\langle\phi_{k_1}^x(t)\big|\hat{\theta}_{+x}\big|\tilde{\Psi}_1(t)\big\rangle, \tag{2.55}$$

which is used in evaluating $b(k_1,k_2,t)$, and derive the equation for its time evolution,

$$\begin{aligned}
&i\partial_t\tilde{b}_1(k_1,n,t)\\
&=\sum_m\big\langle\chi_n^y\big|\hat{H}_y^I-iW_y\big|\chi_m^y\big\rangle\tilde{b}(k_1,m,t)-\sum_m\big\langle\phi_{k_1}^x(t)\big|[\hat{H}_x^V,\hat{\theta}_{+x}]\big|\chi_m^x\big\rangle\big\langle\chi_m^x\big|\big\langle\chi_n^y\big|\tilde{\Psi}_1(t)\big\rangle,\\
&=\sum_m\big\langle\chi_n^y\big|\hat{H}_y^I-iW_y\big|\chi_m^y\big\rangle\tilde{b}(k_1,m,t)-\sum_m\big\langle\phi_{k_1}^x(t)\big|[\hat{H}_x^V,\hat{\theta}_{+x}]\big|\chi_m^x\big\rangle\big\langle\chi_m^x\big|\big\langle\chi_n^y\big|\tilde{\Psi}(t)\big\rangle.
\end{aligned} \tag{2.56}$$

Again in Eq. (2.55), due to the existence of the commutator $[\hat{H}_x^V,\hat{\theta}_{+x}]$, $\big|\tilde{\Psi}_1\big\rangle$ is replaced by $\big|\tilde{\Psi}\big\rangle$, which is the state in practical computation with CAPs included.

The t-SURFF method [14, 15] was originally implemented with the infinite range exterior complex scaling (irECS) method, which can serve as a perfect absorber in time-dependent problems [22]. It can also be implemented with CAPs [16, 23]. Compared with Ref. [15], our derivations here clearly reveal how the introduced CAPs enter the equation for double ionization, as shown in Eq. (2.56).

Chapter 3

Helium in High-Frequency Strong Fields

With the numerical methods discussed in Chapter 2, we can investigate strong-field ionization of the 1D helium model by performing *ab initio* calculations. We focus on ionization by superintense extreme ultraviolet (XUV) laser pulses, which is in the so-called stabilization regime.

3.1 Strong-Field Stabilization

The lowest-order perturbation theory (LOPT) predicts that photon ionization rates increase with intensity I: n-photon ionization rate grows as $\Gamma_n \propto I^n$. However, direct nonperturbative handling of the Schrödinger equation can show that the reverse trend may set in for intense high-frequency lasers: the higher the intensity, the lower the ionization. The phenomenon was first discovered theoretically [3] and later attempts were made to observe it in experiments [24, 25, 26, 27, 28]. It was theoretically predicted that this phenomenon termed as atomic stabilization requires strong laser fields with high frequencies (compared to the ionization potential energy). So the experiments in this area are quite difficult. So far experimental observation of stabilization has only been done in Rydberg atoms, rather than ground-state atoms. It is because only for Rydberg states did the available laser parameters satisfy the theoretical requirement for stabilization.

In contrast, there have been a number of theoretical studies on stabilization, in particular for one-electron systems (see reviews [29, 30]). Comparatively speaking, fewer studies of stabilization in multi-electron systems have been done. Calculations performed in 1D two-electron model systems indicated that correlation effects could reduce the stabilization effect [31]. 3D calculations of helium showed the existence of stabilization in both single and double ionization [32, 33], and it found that 1D models tend to overestimate the effect of correlation. Up to now the dynamics of multi-electron systems in the stabilization regime are still not completely clear, so the motivation of our work is to gain more understanding of the simplest two-electron system, helium, in the presence of high-frequency laser fields.

3.2 High-Frequency Floquet Theory

The high-frequency Floquet theory (HFFT) [34] is a general framework for laser-atom interactions at high frequencies and all intensities. It has been extensively used to study the atomic structure and stabilization in high-frequency fields. Here we briefly introduce the theory, taking a one-electron state as an example. Also, the basic equations for the 1D helium model are given.

Kramers-Henneberger Frame

We start with the TDSE in the laboratory frame within the dipole approximation,

$$i\partial_t\big|\tilde{\Psi}_L\big\rangle = \left\{\frac{1}{2}\left[\hat{p}+\vec{A}(t)\right]^2 + V(\vec{r})\right\}\big|\tilde{\Psi}_L\big\rangle. \tag{3.1}$$

The term containing $\vec{A}^2$ can be eliminated by the phase-factor tranformation

$$\big|\Psi_L\big\rangle = \exp\left[i\int^t dt'\vec{A}^2(t')/2\right]\big|\tilde{\Psi}_L\big\rangle, \tag{3.2}$$

to give

$$i\partial_t\big|\Psi_L\big\rangle = \left[\frac{1}{2}\hat{p}^2 + \vec{A}(t)\cdot\hat{p} + V(\vec{r})\right]\big|\Psi_L\big\rangle. \tag{3.3}$$

A classical electron driven by the field $\vec{A}(t)$ has a quiver motion of vector radius $\vec{\alpha}(t) = \int^t dt'\vec{A}(t')$. By applying to Eq. (3.3) the coordinate translation $\vec{r}\to\vec{r}+\vec{\alpha}(t)$, one can obtain

$$i\partial_t\big|\Psi\big\rangle = \left[\frac{1}{2}\hat{p}^2 + V(\vec{r}+\vec{\alpha}(t))\right]\big|\Psi\big\rangle. \tag{3.4}$$

The space-translated TDSE can be interpreted as characterizing the dynamics of the electron in an accelerated frame of reference, the Kramers-Henneberger (KH) frame [35]. In the KH frame, the center of force has a quiver motion $\vec{\alpha}(t)$ of the classical electron, as indicated by the shift of the potential origin in Eq. (3.4).

Floquet Method

For a monochromatic electric field linearly polarized in the z-direction,

$$\vec{F}(t) = F_0\cos(\omega t)\hat{z}, \tag{3.5}$$

the corresponding vector potential $\vec{A}(t) = -\int^t dt'\vec{F}(t')$ and quiver motion $\vec{\alpha}(t) = \int^t dt'\vec{A}(t')$ are simply

$$\vec{A}(t) = -(F_0/\omega)\sin(\omega t)\hat{z}, \tag{3.6}$$
$$\vec{\alpha}(t) = (F_0/\omega^2)\cos(\omega t)\hat{z}. \tag{3.7}$$

Within the Floquet theory, we can seek a quasiperiodic solution to Eq. (3.3) of the form

$$\big|\Psi(t)\big\rangle = \exp(-iEt)\sum_n\big|\phi_n\big\rangle\exp(-in\omega t), \tag{3.8}$$

and expand the oscillating potential in Fourier series

$$V(\vec{r}+\vec{\alpha}(t)) = \sum_n V_n(\alpha_0;\vec{r})\exp(-in\omega t), \tag{3.9}$$

with

$$V_n(\alpha_0;\vec{r}) = \frac{1}{2\pi}\int_0^{2\pi} d\vartheta V[\vec{r}+\vec{\alpha}(\vartheta/\omega)]\exp(in\vartheta). \tag{3.10}$$

Insertion of Eq. (3.8) and Eq. (3.9) into Eq. (3.3) leads to an infinite set of time-independent coupled equations for the Floquet components $\big|\phi_n\big\rangle$,

$$\left[\frac{1}{2}\hat{p}^2 + V_0 - (E+n\omega)\right]\big|\phi_n\big\rangle = -\sum_{m\neq n} V_{n-m}\big|\phi_m\big\rangle. \tag{3.11}$$

Boundary conditions need to be imposed on the channel states $\big|\phi_n\big\rangle$ to ensure the uniqueness of the solution. These are expressed in terms of the channel momenta k_n defined by $k_n^2/2 = E + n\omega$. To study ionization, these are mostly chosen of the Gamow-Siegert (resonance-state) type, which leads to an eigenvalue problem. Because of the nature of these boundary conditions, the eigenenergy is complex: $E = W - i\Gamma/2$. Briefly speaking, W is the average energy in the field and Γ is its ionization rate.

Lowest Approximation Formulas in HFFT

The HFFT solves the corresponding Floquet system of equations at large ω by succesive iterations of increasing order in ω^{-1}. Here we only briefly discuss the formulas of the zeroth order and the first order, skipping the details of the iteration procedure.

To the lowest order in ω^{-1} and at fixed α_0, the HFFT Floquet system reduces to a single equation, the structure equation

$$\left[\frac{1}{2}\hat{p}^2 + V_0(\vec{\alpha}_0;\vec{r})\right]u_n = W_n u_n, \tag{3.12}$$

From Eq. (3.10) we know that V_0 is the time average of the oscillating potential. In the KH frame the potential has an oscillating bahavior. As ω is supposed large, the electron will not react to the rapid oscillations of the potential, but rather to its time average. In the high-frequency limit $\omega \to \infty$, the energy W is real, which means that there is no ionization. For a linearly polarized field, at sufficiently large α_0, the eigenfunction of any state splits into two practically nonoverlapping parts (atomic dichotomy) due to the two-center character of the dressed potential V_0 [34, 36, 37].

The first iteration within the HFFT allows for ionization [38]. For the partial n-photon ionization rates it gives

$$d\Gamma_n/d\Omega = k_n\left|f_n(k)\right|^2 \tag{3.13}$$

with the amplitude

$$f_n(k) = -\frac{1}{2\pi}\big\langle u_{k_n}\big|V_n\big|u_0\big\rangle \tag{3.14}$$

Here $\big|u_{k_n}\big\rangle$ is a contnuum state of Eq. (3.12) with asymptotic momentum k_n.

The zeroth-order and first-order formulas are most frequently used in describing the laser-dressed atomic structure and the ionization rate, while the higher-order corrections

are usually neglected. A pragmatic convergence criterion for the HFFT iteration scheme was shown to be the high-frequency condition, $\omega \gg W(\alpha_0)$, where $W(\alpha_0)$ is an average excitation energy for the manifold of the initial state. Most often, $W(\alpha_0)$ is of the order of magnitude of the largest binding energy of the manifold. One should note that this is a sufficient condition: HFFT results may apply even when it is not satisfied.

HFFT for 1D Helium

Following Eq. (2.1), the space-translated TDSE of our 1D helium model reads,

$$i\partial_t \big|\Psi\big\rangle = \Big\{\hat{T}_x + \hat{T}_y + V_x[x+\alpha(t)] + V_y[y+\alpha(t)] + V_{xy}\Big\}\big|\Psi\big\rangle. \tag{3.15}$$

The corresponding structure equation is

$$\Big\{\hat{T}_x + \hat{T}_y + V_0(\alpha_0;x) + V_0(\alpha_0;y) + V_{xy}\Big\}\big|\Phi\big\rangle = W(\alpha_0)\big|\Phi\big\rangle. \tag{3.16}$$

With the initial and final states denoted by $\big|\Phi_i\big\rangle$ and $\big|\Phi_f\big\rangle$, which are both solutions to Eq. (3.16), the n-photon rate is given by

$$\Gamma_n = 2\pi \Big|\big\langle\Phi_f\big|[V_n(\alpha_0;x) + V_n(\alpha_0;y)]\big|\Phi_i\big\rangle\Big|^2 \tag{3.17}$$

with conservation of energy requiring $W_i + n\omega = W_f$. To study the single and double ionization, we may choose the final state $\big|\Phi_f\big\rangle$ to be an ionic state and a double continuum state, respectively.

3.3 Results and Discussions

Energy Levels

Before discussing the strong-field ionization of helium, we first provide some information about the energy levels of the 1D helium model. This may help us understand the role of laser frequencies and illustrate the motivation of our study.

A δ-like dipole excitation spectrum can help identify some energy levels of the system. Choosing the ground state as the initial state, we excite the system with a δ-like dipole kick ($F_0 = 0.001, t_0 = 1, \sigma = 0.1$),

$$F(t) = F_0 \exp\left[-\frac{(t-t_0)^2}{2\sigma^2}\right], \tag{3.18}$$

and record the dipole response $d(t) = \big\langle\Psi(t)\big|[x(t)+y(t)]\big|\Psi(t)\big\rangle$ over a long time (4000 a.u.). A Fourier transform with respect to time, $S(\omega) = |\mathcal{F}\{d(t)\}|^2$, gives the dipole excitation spectrum, as shown in Fig. 3.1.

In Fig. 3.2, the energies of the ground state and the first excited state are calculated by imaginary time propagation, while the single ionization channel energies are calculated by diagonalizing the ionic hamiltonian. Two doubly excited states, identified from the dipole excitation spectrum are also shown.

Due to the 1D model, single electron wavefunction can be only even or odd. We denote single electron states by $\big|1e\big\rangle$, $\big|2o\big\rangle$, $\big|3e\big\rangle$, $\big|4o\big\rangle$, etc. On the basis of electron configurations, we can use $\big|1e1e\big\rangle$ for the ground state and $\big|1e2o\big\rangle$ for the first excited state. [1] The ground state $\big|1e1e\big\rangle$ has two equivalent electrons while the first excited state $\big|1e2o\big\rangle$ has two non-equivalent electrons.

[1] $\big|1e1e\big\rangle$ and $\big|1e2o\big\rangle$ should be understood as the dominating configurations.

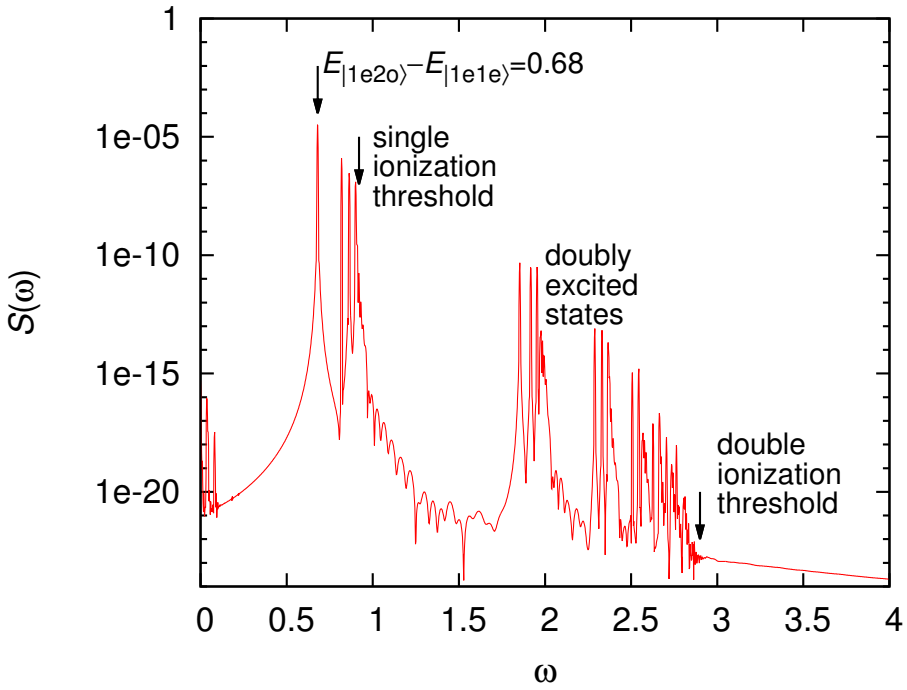

Figure 3.1: Dipole excitation spectrum $S(\omega)$ of the 1D helium model.

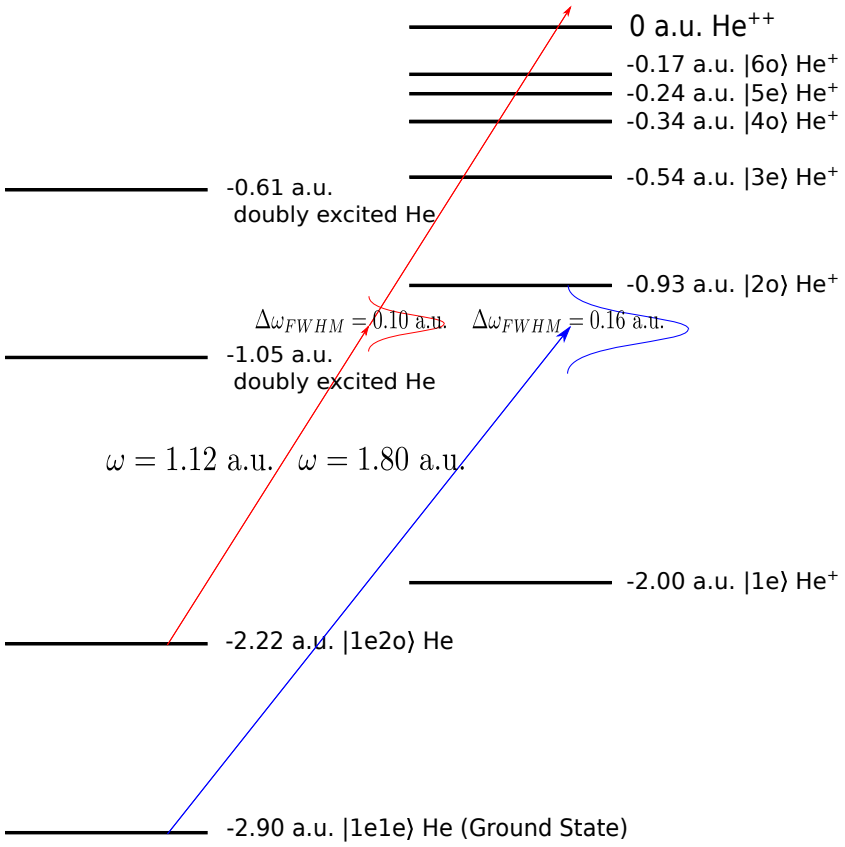

Figure 3.2: Energy levels of the 1D helium model, including the ground state, the spin-singlet first excited state, the lowest 6 single ionic states, two doubly excited states and the double ionization threshold. The red and blue arrows indicate two laser frequencies used, with the their spectral bandwidths also shown.

Computational Parameters

We use a short laser pulse (5 cycles) with a Gaussian envelope, defined by its vector potential,

$$A(t) = (F_0/\omega)\exp\left(-4\ln 2\frac{t^2}{t_{FWHM}^2}\right)\sin(\omega t), \tag{3.19}$$

and the number of cycles is defined as $N_c = \omega t_{FWHM}/(2\pi)$.

We can choose the ground state or the first excited state as the initial state. For both the ground state and the first excited state, we do calculations in two cases: (1) One-photon absorption can only open the $|1e\rangle$ He^+ channel while two-photon absorption can open all the channels, including double ionization. (2) One-photon absorption can open all the channels, including double ionization. For the ground state $|1e1e\rangle$, we use $\omega_1 = 1.80$ for case (1) and $\omega_1 = 3.90$ for case (2). For the excited state $|1e2o\rangle$, we use $\omega_1 = 1.12$ for case (1) and $\omega_1 = 3.22$ for case (2). The case (1) is also shown in Fig. 3.2.

For two-electron atoms, stabilization has been studied for total ionization, single ionization and double ionization [39, 31, 40, 32, 33]. To our knowledge, there is still no research on the ionization in different single ionization channels, i.e., the populations of different residual ionic states have not been investigated for single ionization. Compared with total ionization probability, we believe that the probabilities for different channels may provide more information. So the t-SURFF method is applied to study the channel-resolved probabilities.

The simulation box is defined as $\{|x| < 120, |y| < 120\}$, with 120 finite elements and 9 DVR functions in each element for each electron. The TDSE is solved with a time step $\Delta t = 0.002$, by using the Arnoldi-Lanczos propagator with a Krylov space of dimension $L = 9$. In the RTP, the CAPs are given by Eq. (2.37) in Chapter 2, with $r_c = 65$. In the t-SURFF method, the surfaces are placed at $r_s = 60$.

Identification of Stabilization

In Fig. 3.3 and Fig. 3.4 we plot the ionization probabilities (the total ionization probability and the probabilities of individual channels) versus the field strength. For high intensities, the total ionization probabilities are close to 1. From the insets in Fig. 3.3 and Fig. 3.4, we find that stabilization actually occurs.

At low field strengths ($F_0 < 1$), the $|1e\rangle$ He^+ channel ionization dominates for the ground state $|1e1e\rangle$. For the excited state $|1e2o\rangle$, both the $|1e\rangle$ He^+ channel and the $|2o\rangle$ He^+ channel are important. We may understand these on the basis of an independent-electron picture, i.e., $|1e1e\rangle \to |1e\varepsilon p\rangle$ channel means that one of the two equivalent is freed while the other is bound; $|1e2o\rangle \to |1e\varepsilon p\rangle$ channel means that the outer electron is freed while the inner one is bound; $|1e2o\rangle \to |2o\varepsilon p\rangle$ channel means that the inner electron is freed while the outer one is bound. [2] So at low field strengths the main dynamics is that only one electron is freed while the other one is still bound in the same state. For the ground state $|1e1e\rangle$ with two equivalent electrons, only $|1e1e\rangle \to |1e\varepsilon p\rangle$ dominates. For the excited state $|1e2o\rangle$ with two nonequivalent (inner and outer) electrons, both $|1e2o\rangle \to |1e\varepsilon p\rangle$ and $|1e2o\rangle \to |2o\varepsilon p\rangle$ can be important.

For high field strengths ($F_0 > 2$), the double ionization dominates, which is (at least) a two-photon process. The two-photon double ionization (TPDI) has been studied both theoretically [41, 42, 43] and experimentally [44, 45] in recent years. Some studies discuss

[2] Here we use notation $|\varepsilon p\rangle$ for a free electron with energy ε and proper parity p (e or o).

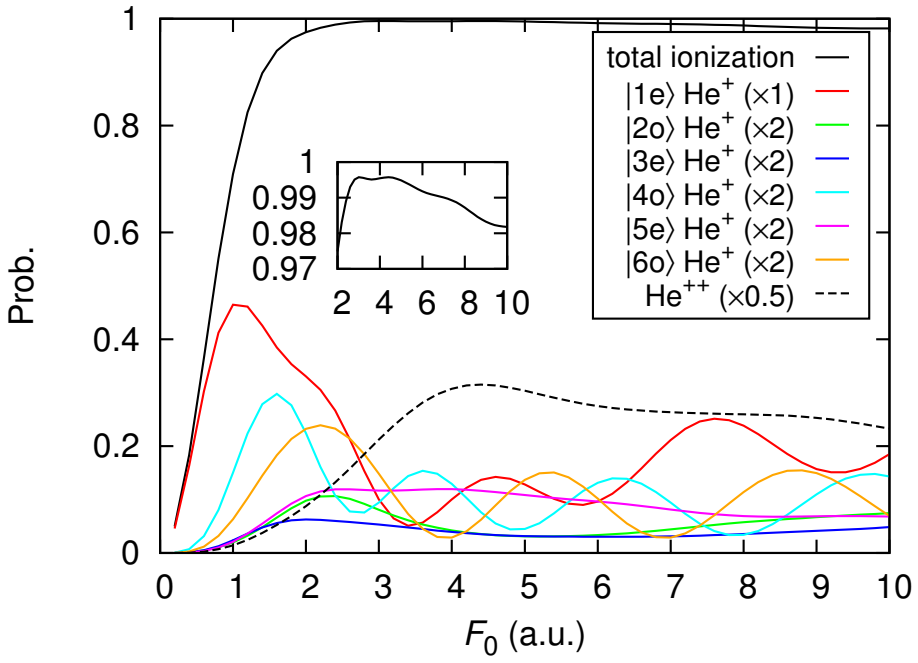

Figure 3.3: Total, double and the lowest 6 single-channel ionization probabilities of the ground state helium $|1e1e\rangle$ versus electric field strength F_0, for a 5-cycle pulse with $\omega = 1.80$. Inset: zoom-in of the total ionization probability.

the sequential and nonsequential regimes at low or intermediate laser intensities [43, 46, 47]. However, researches on the TPDI in the stabilization regime are still scarce [32, 33].

The oscillation behavior of the ionization probabilities versus the field strength was observed and discussed for one-electron systems [48, 49], and was attributed to the two-center character of the dressed atomic wavefunction. For our two-electron system, the oscillating probabilities in different channels are much more complicated, which would need more investigations to be understood.

For high frequencies of case (2), the total ionization probabilities are much smaller than those of case (1). Stabilization can be clearly observed from Fig. 3.5 and Fig. 3.6. This is quite natural since stabilization is a high-frequency phenomenon according to the HFFT. Dressed in a laser field with a higher frequency, the atom becomes more easily stabilized.

From Fig. 3.5, we find that the $|1e\rangle$ He^+ channel dominates for the ground state $|1e1e\rangle$ while the other channels give much smaller contribution to the total ionization probability. An interesting phenomenon appears in Fig. 3.6, i.e., $|3e\rangle$ He^+ channel dominates for the excited state $|1e2o\rangle$, which calls for future studies.

Finally, we solve the structure equation Eq. (3.16) and obtain the laser dressed energy levels. As Fig. 3.7 shows, the high-frequency laser actually changes the average energy of all the states. This is the lowest order calculation within the HFFT, and will be continued in the future, which may serve as an explanation of the results shown here.

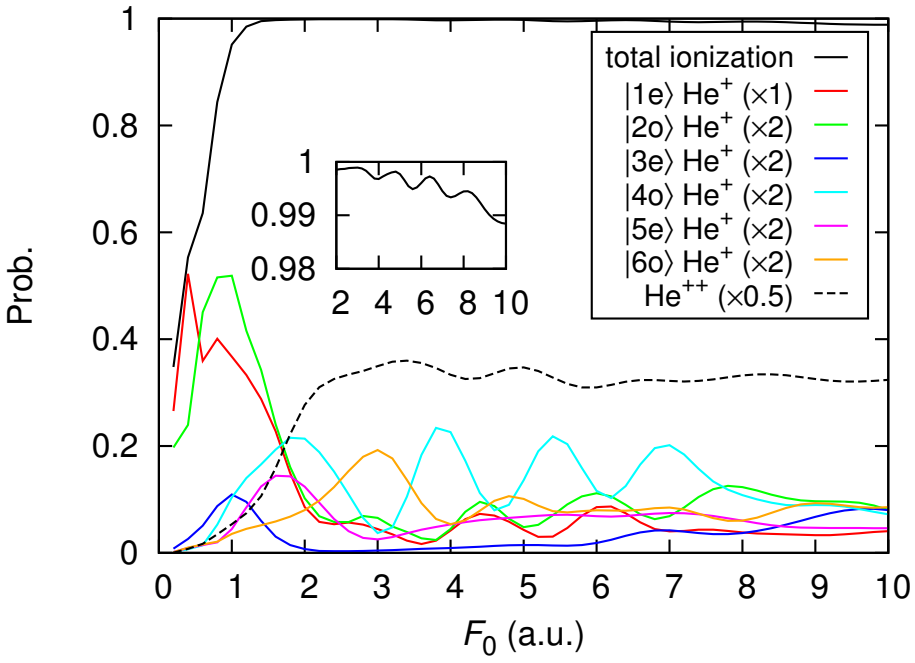

Figure 3.4: Total, double and the lowest 6 single-channel ionization probabilities of the excited state helium $|1e2o\rangle$ versus electric field strength F_0, for a 5-cycle pulse with $\omega = 1.12$. Inset: zoom-in of the total ionization probability.

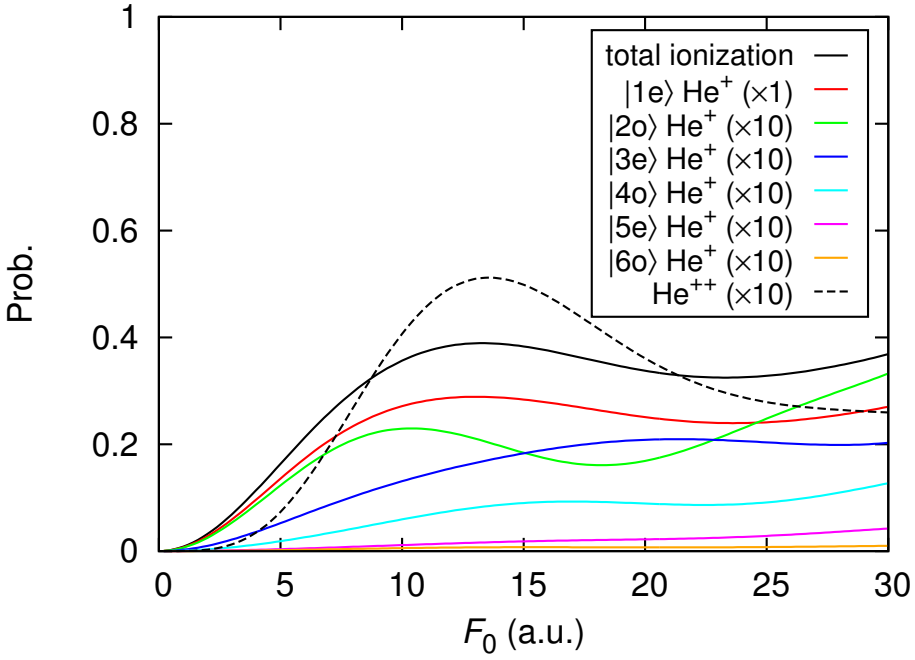

Figure 3.5: Total, double and the lowest 6 single-channel ionization probabilities of the ground state helium $|1e1e\rangle$ versus electric field strength F_0, for a 5-cycle pulse with $\omega = 3.90$.

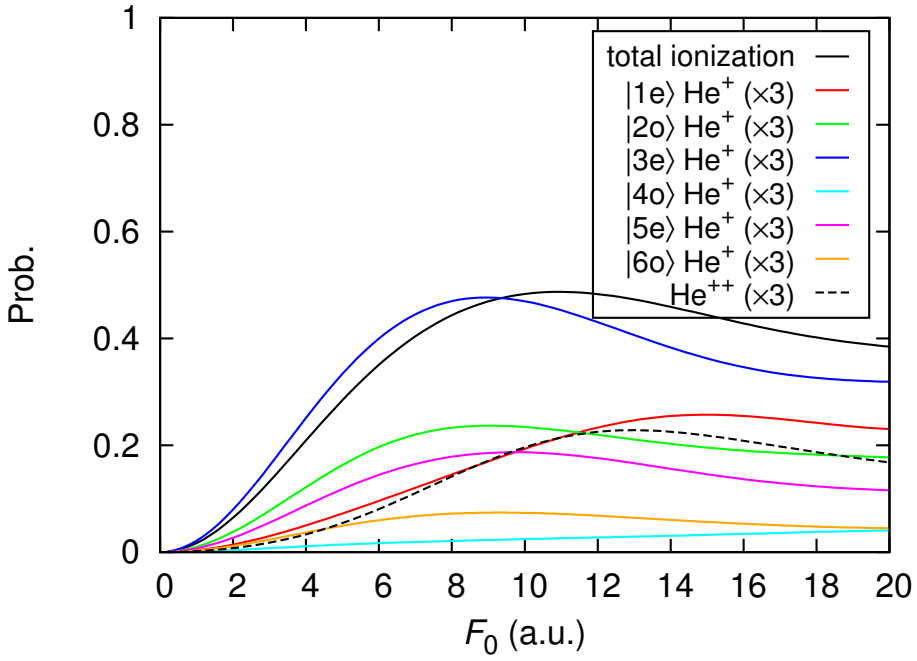

Figure 3.6: Total, double and the lowest 6 single-channel ionization probabilities of the excited state helium $|1e2o\rangle$ versus electric field strength F_0, for a 5-cycle pulse with $\omega = 3.22$.

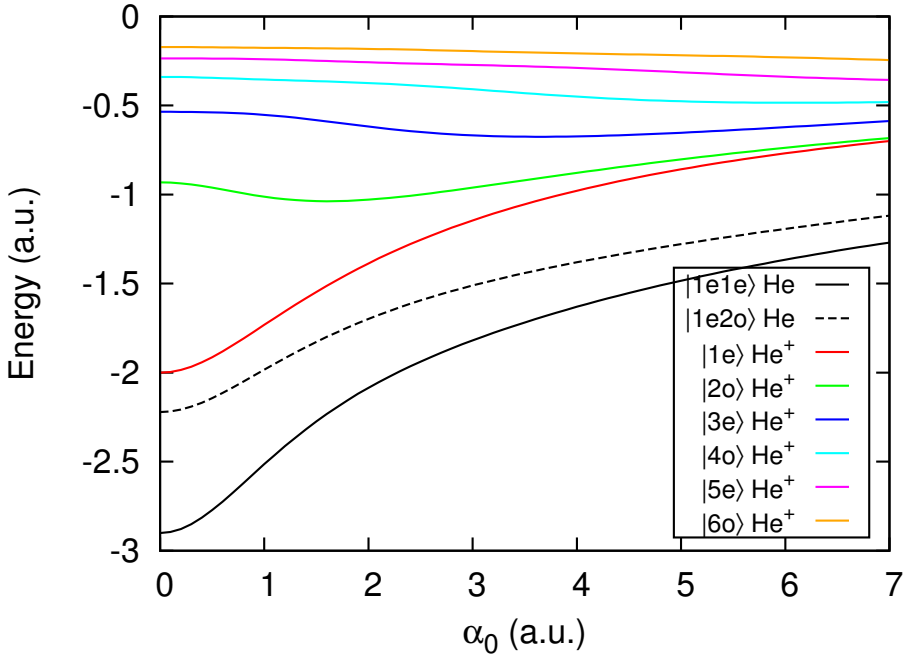

Figure 3.7: Dressed energy levels of the high-frequency structure equation versus α_0

Chapter 4

Summary and Outlook

4.1 Summary

Here is a summary of my work during part A of my Ph.D. studies.

By using an FEDVR basis set and the Arnoldi-Lanczos time propagator, we have made a FORTRAN code for solving the TDSE of a 1D two-electron system such as helium. With CAPs as absorbers at the grid boundaries, we implement the t-SURFF method to extract spectra of single and double ionization. This allows us to study the photoelectron spectra with a small simulation volume, even in the strong-field regime.

By applying the TDSE solver to a 1D helium model, we study the strong-field ionization of helium exposed to short XUV laser pulses. On the basis of the energy levels of this 1D model, we choose the ground state $\left|1e1e\right\rangle$ and the first excited state $\left|1e2o\right\rangle$ as two initial states, and investigate how the total and channel-resolved ionization probabilities change with the laser field strength. For the laser frequency, we consider two cases: (1) the system can only ionize into the $\left|1e\right\rangle$ He^+ channel by absorbing one photon energy, but it can be doubly ionized by absorbing two photon energy; (2) double ionization can occur with only one photon absorption.

In both cases we observe atomic stabilization, i.e., decreasing ionization probabilities with increasing laser field strength. However, the ionization probabilities into different channels are much more complicated, which have not been completely understood, and will be work for the immediate future.

For the laser frequencies of case (1), double ionization dominates at high laser intensity for both the ground state $\left|1e1e\right\rangle$ and the excited state $\left|1e2o\right\rangle$, which means that the two photon double ionization may be the most important process in the strong-field interaction regime. The $\left|1e\right\rangle$ He^+ channel dominates at low laser intensity for both the ground state $\left|1e1e\right\rangle$ and the excited state $\left|1e2o\right\rangle$. In addition, the $\left|2o\right\rangle$ He^+ channel is the second important at low laser intensity for the excited state $\left|1e2o\right\rangle$, We interpret this as the process $\left|1e2o\right\rangle \rightarrow \left|2o\varepsilon p\right\rangle$, in which the inner electron is freed while the outer one is bound. However, the results for the laser frequencies of case (2) are not fully understood, i.e., the $\left|1e\right\rangle$ He^+ channel dominates for the ground state $\left|1e1e\right\rangle$ while the $\left|3e\right\rangle$ He^+ channel dominates for the excited state $\left|1e2o\right\rangle$. This interesting phenomenon may require more investigations.

Based on the HFFT, which is extensively used in the stabilization regime, we also perform the lowest-order calculation within this non-perturbative theory and obtain the laser dressed energy levels. Calculations on the basis of the HFFT will be continued in the future.

4.2 Outlook

In the nearest future, we will continue doing more calculations in the stabilization regime. We would like to implement the first-order HFFT calculations and compare those with our *ab initio* calculations, since the HFFT may offer an interpretation and help us to understand the results. The HFFT applies for the long pulse limit, so we may extend our *ab initio* calculations to longer laser pulses, This may also reveal the role of the pulse duration in the dynamics.

There are also a number of open questions that can be studied with our 1D two-electron TDSE solver. For example, how are the different channels coupled with one another in the stabilization regime? What is the role of the doubly excited states in the strong-field ionization? Will any new dynamics appear when extending attosecond experiments, such as streaking [50], to the strong-field regime?

Afterwards, we plan to perform calculations on multi-electron atoms interacting with laser fields in full dimensions. On the one hand, we may extend the two electron TDSE solver to 3D. Combined with the t-SURFF method, the photoelectron spectra can be computed with a small simulation volume. On the other hand, we plan to resort to a general multi-electron scheme based on quantum chemistry, such as TD-RASCI or TD-RASSCF. Implementation of the t-SURFF method in that approach will be a meaningful task for the future.

Bibliography

[1] P. Agostini, F. Fabre, G. Mainfray, G. Petite, and N. K. Rahman, *Phys. Rev. Lett.* 42, 1127–1130, 1979.

[2] P. B. Corkum, *Phys. Rev. Lett.* 71, 1994–1997, 1993.

[3] M. Pont and M. Gavrila, *Phys. Rev. Lett.* 65, 2362–2365, 1990.

[4] F. Krausz and M. Ivanov, *Rev. Mod. Phys.* 81, 163–234, 2009.

[5] K. C. Kulander, K. J. Schafer, and J. L. Krause, *Int. J. Quantum Chem.* 40, 415–429, 1991.

[6] P. G. Burke and V. M. Burke, *J. Phys. B* 30, L383, 1997.

[7] M. A. Lysaght, P. G. Burke, and H. W. van der Hart, *Phys. Rev. Lett.* 101, 253001, 2008.

[8] M. A. Lysaght, H. W. van der Hart, and P. G. Burke, *Phys. Rev. A* 79, 053411, 2009.

[9] J. Caillat, J. Zanghellini, M. Kitzler, O. Koch, W. Kreuzer, and A. Scrinzi, *Phys. Rev. A* 71, 012712, 2005.

[10] D. J. Haxton, K. V. Lawler, and C. W. McCurdy, *Phys. Rev. A* 83, 063416, 2011.

[11] D. Hochstuhl and M. Bonitz, *Phys. Rev. A* 86, 053424, 2012.

[12] H. Miyagi and L. B. Madsen, *Phys. Rev. A* 87, 062511, 2013.

[13] H. Miyagi and L. B. Madsen, *Phys. Rev. A* 89, 063416, 2014.

[14] L. Tao and A. Scrinzi, *New J. Phys.* 14, 013021, 2012.

[15] A. Scrinzi, *New J. Phys.* 14, 085008, 2012.

[16] L. Yue and L. B. Madsen, *Phys. Rev. A* 88, 063420, 2013.

[17] J. C. Light and T. Carrington Jr, *Adv. Chem. Phys.* 114, 263–310, 2000.

[18] W. H. Press, *Numerical recipes 3rd edition: The art of scientific computing*, 2007.

[19] T. N. Rescigno and C. W. McCurdy, *Phys. Rev. A* 62, 032706, 2000.

[20] J. Muga, J. Palao, B. Navarro, and I. Egusquiza, *Phys. Rep.* 395, 357–426, 2004.

[21] L. B. Madsen, L. A. A. Nikolopoulos, T. K. Kjeldsen, and J. Fernández, *Phys. Rev. A* 76, 063407, 2007.

[22] A. Scrinzi, *Phys. Rev. A* 81, 053845, 2010.

[23] A. Karamatskou, S. Pabst, Y.-J. Chen, and R. Santra, *Phys. Rev. A* 89, 033415, 2014.

[24] M. P. de Boer, J. H. Hoogenraad, R. B. Vrijen, L. D. Noordam, and H. G. Muller, *Phys. Rev. Lett.* 71, 3263–3266, 1993.

[25] R. R. Jones, D. W. Schumacher, and P. H. Bucksbaum, *Phys. Rev. A* 47, R49–R52, 1993.

[26] M. P. de Boer, J. H. Hoogenraad, R. B. Vrijen, R. C. Constantinescu, L. D. Noordam, and H. G. Muller, *Phys. Rev. A* 50, 4085–4098, 1994.

[27] J. H. Hoogenraad, R. B. Vrijen, and L. D. Noordam, *Phys. Rev. A* 50, 4133–4138, 1994.

[28] N. J. van Druten, R. C. Constantinescu, J. M. Schins, H. Nieuwenhuize, and H. G. Muller, *Phys. Rev. A* 55, 622–629, 1997.

[29] M. Gavrila, *J. Phys. B* 35, R147, 2002.

[30] A. M. Popov, O. V. Tikhonova, and E. A. Volkova, *J. Phys. B* 36, R125, 2003.

[31] D. Bauer and F. Ceccherini, *Phys. Rev. A* 60, 2301–2307, 1999.

[32] T. Birkeland, R. Nepstad, and M. Førre, *Phys. Rev. Lett.* 104, 163002, 2010.

[33] S. A. Sørngård, S. Askeland, R. Nepstad, and M. Førre, *Phys. Rev. A* 83, 033414, 2011.

[34] M. Gavrila and J. Z. Kamiński, *Phys. Rev. Lett.* 52, 613–616, 1984.

[35] W. C. Henneberger, *Phys. Rev. Lett.* 21, 838–841, 1968.

[36] M. Pont, N. R. Walet, M. Gavrila, and C. W. McCurdy, *Phys. Rev. Lett.* 61, 939–942, 1988.

[37] M. Pont, N. R. Walet, and M. Gavrila, *Phys. Rev. A* 41, 477–494, 1990.

[38] M. Gavrila, *Atoms in intense laser fields*, 1992.

[39] M. Gavrila and J. Shertzer, *Phys. Rev. A* 53, 3431–3443, 1996.

[40] E. Volkova, V. Gridchin, A. Popov, and O. Tikhonova, *JETP* 99, 320–327, 2004.

[41] J. Colgan and M. S. Pindzola, *Phys. Rev. Lett.* 88, 173002, 2002.

[42] J. Feist, S. Nagele, R. Pazourek, E. Persson, B. I. Schneider, L. A. Collins, and J. Burgdörfer, *Phys. Rev. Lett.* 103, 063002, 2009.

[43] A. Liu and U. Thumm, *Phys. Rev. Lett.* 115, 183002, 2015.

[44] Y. Nabekawa, H. Hasegawa, E. J. Takahashi, and K. Midorikawa, *Phys. Rev. Lett.* 94, 043001, 2005.

[45] A. Rudenko, L. Foucar, M. Kurka, T. Ergler, K. U. Kühnel, Y. H. Jiang, A. Voitkiv, B. Najjari, A. Kheifets, S. Lüdemann, T. Havermeier, M. Smolarski, S. Schössler, K. Cole, M. Schöffler, R. Dörner, S. Düsterer, W. Li, B. Keitel, R. Treusch, M. Gensch, C. D. Schröter, R. Moshammer, and J. Ullrich, *Phys. Rev. Lett.* 101, 073003, 2008.

[46] W.-C. Jiang, J.-Y. Shan, Q. Gong, and L.-Y. Peng, *Phys. Rev. Lett.* 115, 153002, 2015.

[47] S. Selstø, X. Raynaud, A. S. Simonsen, and M. Førre, *Phys. Rev. A* 90, 053412, 2014.

[48] Q. Su, B. P. Irving, and J. H. Eberly, *Las. Phys.* 7, 568–573, 1997.

[49] M. Dörr and R. M. Potvliege, *J. Phys. B* 33, L233, 2000.

[50] J. C. Baggesen and L. B. Madsen, *Phys. Rev. Lett.* 104, 043602, 2010.